RSC Advances

This is an *Accepted Manuscript*, which has been through the Royal Society of Chemistry peer review process and has been accepted for publication.

Accepted Manuscripts are published online shortly after acceptance, before technical editing, formatting and proof reading. Using this free service, authors can make their results available to the community, in citable form, before we publish the edited article. This *Accepted Manuscript* will be replaced by the edited, formatted and paginated article as soon as this is available.

You can find more information about *Accepted Manuscripts* in the Information for Authors.

Please note that technical editing may introduce minor changes to the text and/or graphics, which may alter content. The journal's standard Terms & Conditions and the Ethical guidelines still apply. In no event shall the Royal Society of Chemistry be held responsible for any errors or omissions in this *Accepted Manuscript* or any consequences arising from the use of any information it contains.

ROYAL SOCIETY OF CHEMISTRY

www.rsc.org/advances

A table of contents

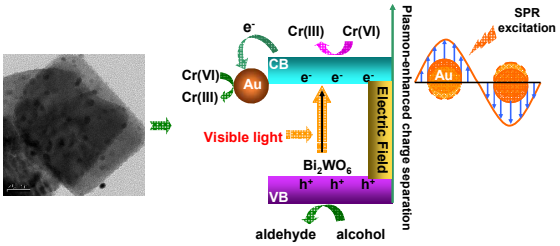

Deposition of Au NPs enhances photocatalytic activity toward selective oxidation of alcohol in water and Cr(VI) reduction over Bi_2WO_6 nanosheets.

RSC Advances Accepted Manuscript

RSC Advances

Enhanced photocatalytic activities of visible-light driven green synthesis in water and environmental remediation on Au/Bi_2WO_6 hybrid nanostructures

Juan Yang*, Xiaohan Wang, Yumei Chen, Jun Dai*, Shihao Sun

Received (in XXX, XXX) Xth XXXXXXXXX 20XX, Accepted Xth XXXXXXXXX 20XX
DOI: 10.1039/xxxxxxxx/

Abstract: A series of Au/Bi_2WO_6 nanocomposites with different weight ratios of Au were fabricated via a hydrothermal combined with a rapid reduction-deposition method. Au/Bi_2WO_6 nanocomposites are proven to serve as selective visible light photocatalysts toward aerobic oxidation of benzylic alcohols and reduction of heavy ions Cr(VI), instead of being nonselective in water. Loading Au NPs greatly enhances the photocatalytic activity of Bi_2WO_6 for the selective oxidation of alcohols and reduction of heavy metal ions. The enhancing effect is dependent on the weight ratios of Au to Bi_2WO_6 in the hybrid nanostructures. The optimal catalysts for alcohol oxidation and Cr(VI) reduction are 2.0 wt% and 1.0 wt% Au/Bi_2WO_6, respectively. Furthermore, we find that loading Au results in an obvious increase in photo-induced generation of charge carriers and active radicals determined by electron spin resonance spectroscopy (ESR). ESR signals denoting photogenerated holes and catalytic activity of alcohol oxidation have a similar dependence on the amounts of Au loading. Besides, the generation and transfer of photogenerated electrons induced by Au loading, as well as the relationship with photocatalytic activity of Cr(VI) reduction, have been examined using the photoelectrochemical characterizations. The possible roles of Au deposition in improving the photocatalytic redox activity of Bi_2WO_6 are also discussed.

Keywords: Visible-light photocatalysis, Bi_2WO_6, Au NPs, selective oxidation, Cr(VI) reduction

1. Introduction

Semiconductor photocatalysis has attracted significant attention due to its promising application in environmental benign organic synthesis, production of hydrogen from water, and degradation of toxic pollutants.[1-3] Since the photocatalytic process involves the generation of charge carriers induced by light, an

RSC Advances Accepted Manuscript

ideal photocatalyst should have both a wide photo-absorption range and a low recombination rate of photogenerated charge carriers. Several attempts have been made to engineer the band structure of semiconductor to extend the spectral responsive range by doping nonmetal or metal ions,[4] localize charge carriers on the surface of semiconductor by adding inorganic sensitizers or dyes,[5] and to construct heterostructures to improve the charge separation efficiency of photocatalysts,[6,7] while more work has focused on developing novel photo-functional materials that can harvest visible-light photons and convert them to chemical energy.[8]

It has been previously reported that loading of an appropriate co-catalyst on traditional photocatalysts (such as TiO_2, ZnO, and SnO_2) can effectively reduce the surface recombination of photogenerated electron-hole pairs and significantly enhance the photocatalytic activity.[9] More importantly, for the certain metallic nanostructures including Au and Ag nanoparticles (NPs), the surface plasmon resonance (SPR) localized at the conduction band of metal nanostructures generally overlaps with the solar spectrum and has been employed to promote the efficiency of photocatalysis under visible light irradiation.[10-12] The electrons in metal NPs might be excited by the localized SPR with visible light absorption and subsequently transferred to the conduction band of the attached semiconductors. The electrons transferred to the surface of semiconductors and the holes remaining on the surface of metal NPs can act as redox centers to initiate photocatalytic reactions.[13] Alternatively, the SPR on metal nanostructures may enhance the local electric field of neighboring semiconductors, and therefore, enhance the photocatalytic efficiency of semiconductors.[14]

As one of the simplest Aurivillius oxides with layered structure, Bi_2WO_6 is special for its good photocatalytic performance under visible light irradiation.[15-17] However, bare Bi_2WO_6 can be excited by the irradiation from UV light to visible light with wavelength of shorter than ca. 450 nm,[18] which only occupies a small part of the solar spectrum. Moreover, the rapid recombination of photoinduced electron-hole pairs seriously limits the energy conversion efficiency of Bi_2WO_6 photocatalytic system. Xue et al. have reported that loading of Ag NPs could greatly improve the photocatalytic activity of Bi_2WO_6 in both the decolorization of dye RhB and desulfurization of thiophene.[19] The loaded Ag NPs acted as the electron receptor on the surface of Bi_2WO_6, which inhibited the recombination of photogenerated charge carriers and improved the photocatalytic activity. However, the heterogeneous nanostructures between plasmonic Au NPs and Bi_2WO_6 nanosheets, the improved photocatalytic performance compared with the individual

RSC Advances Accepted Manuscript

Bi_2WO_6, and the possible enhanced mechanism were not investigated before.

Water is a more economic and environmentally viable solvent for the organic reaction. The aqueous-phase photocatalysis has received wide research interest, mainly in the nonselective degradation of pollutants for the environmental cleanup.[20-22] In recent years, with increasingly severe environmental limitations on chemical processes, the aqueous-phase photocatalysis has been utilized in some other processes, including selective organic synthesis.[23-28] For example, Palmisano's group has carried out aqueous-phase selective oxidation of benzyl alcohols to benzaldehydes with selectivities of 45-74% over the home-prepared rutile TiO_2.[28-30] Xu et al., has reported that the flower-like Bi_2WO_6 can selectively oxidizing glycerol and benzylic alcohols in water under ambient conditions.[26,27] The reported researches substantiate the versatile capability of semiconductor-based photocatalysis to drive the selective redox reactions in water.[23-30]

In this study, we reported the effective photocatalytic selective oxidation of alcohols in water, a green solvent in organic chemistry, over Au/Bi_2WO_6 hybrid nanostructures with different weight ratios of Au under visible light irradiation (λ>400 nm). On the other hand, the photocatalytic activity of Cr(VI) reduction over Bi_2WO_6 was substantially improved after Au NPs loading. The relationships between the photo-induced generation of charge carriers and photocatalytic activity of benzyl alcohol oxidation or Cr(VI) reduction were investigated over Au/Bi_2WO_6 nanocomposites by using ESR and photoelectrochemical techniques. The optimal amounts of Au NPs loaded in the Au/Bi_2WO_6 hybrid nanostructures were determined for the alcohol oxidation and Cr(VI) reduction, respectively. Based on these results, the possible roles of Au deposition in improving the photocatalytic activity of Bi_2WO_6 were also discussed. It is hoped that this work can draw attention to synthesize more efficient nanocomposite photocatalysts for solar energy conversion, especially in the field of diverse redox processes in water under the framework of green chemistry.

2. Experimental Section

2.1 Materials

L-lysine and benzylic alcohols were obtained from J&K Scientific Ltd., P. R. China. 5,5-dimethyl-1-pyrroline N-oxide (DMPO) and 2,2,6,6-tetramethylpiperidine-1-oxyl (TEMPO) were purchased from TCI (Shanghai) Development Ltd. Bismuth nitrate pentahydrate ($Bi(NO_3)_3 \cdot 5H_2O$), sodium

RSC Advances Accepted Manuscript

tungstate dehydrate ($Na_2WO_4 \cdot 2H_2O$), nitric acid (HNO_3), ethylene glycol, chloroauric acid hydrated, sodium hydroxide (NaOH), and sodium borohydride ($NaBH_4$) were AR reagents purchased from Beijing Chemical Works, P. R. China. All chemicals were used as received without further purification and all aqueous solutions were prepared with ultrapure water obtained from Millipore system.

2.2 Catalysts preparation

Bi_2WO_6 nanosheets were synthesized following a modified hydrothermal method. Typically, 5mmol of $Bi(NO_3)_3 \cdot 5H_2O$ was dissolved in 2.5 ml of 20% HNO_3 (vol %) aqueous solution. Then, 20ml of 0.125 mol/L $Na_2WO_4 \cdot 2H_2O$ ethylene glycol solution was added, followed by vigorous stirring 1h to obtain an uniform suspension. The pH of the suspension was adjusted to 7.5 with 0.1 mol/L NaOH. Subsequently, the mixed solution was transferred to 100ml Teflon-sealed autoclave and maintained at 453K for 5h. The resulting sample was recovered by filtration, washed by water and alcohol, and fully dried at 333K in oven to get Bi_2WO_6 nanosheets sample.

The Au/Bi_2WO_6 catalysts were prepared by a sonication-assisted reduction method according to the literature.[31] In a typical preparation of Au/Bi_2WO_6 catalyst (2.0 wt%), 0.5 g Bi_2WO_6 was put in 5.0 ml deionized water, and 5.3 ml of 0.01 mol/L $HAuCl_4$ and 6.0 ml of 0.01 mol/L lysine were added subsequently. The pH of the suspension was adjusted to 5-6 with 0.1 mol/L NaOH. Thereafter, the suspension was subjected to ultrasonication for 20 s. Freshly prepared 5.3 ml $NaBH_4$ (0.1 mol/L, 5-10 times the Au molar number) was injected during the sonication. The products were collected by centrifugation, washed thoroughly with water, and dried at 333 K overnight. The obtained powders were calcined in a muffle furnace at 573 K for 1h. The as-prepared composite catalyst was referred to as 2.0 wt% Au/Bi_2WO_6. A series of Au/Bi_2WO_6 composites with different weight ratios of Au to Bi_2WO_6 were prepared by changing the amounts of $HAuCl_4$ solution.

2.3 Catalysts characterization

The X-ray diffraction (XRD) measurements were performed on a D8 Advance diffractometer (Bruker) with Cu Kα radiation ($\lambda = 0.15405$ nm) in the range of 10-80° (2θ). Transmission electron microscopy (TEM) and high resolution transmission electron microscope (HRTEM) images were obtained with a FEI Tecnai G2 high-resolution transmission electron microscope operating at 200kV. UV-vis diffuse-reflectance spectra (UV-vis DRS) were obtained on an UV-vis spectrophotometer (UV-2550, Shimadzu, Japan) at room temperature and transformed to the absorption spectrum according to the Kubelka-Munk relationship.

RSC Advances Accepted Manuscript

$BaSO_4$ was used as a reflectance standard in the UV-vis diffuse-reflectance experiments. XPS measurements were performed on a Thermo Scientific ECALAB 250xi system with Mg Kα source. All the binding energies were calibrated by C1S peak at 284.8 eV of the surface adventitious carbon. Energy-dispersive X-ray (EDX) spectroscopy being attached to scanning electron microscopy (SEM, Hitachi S4800) was used to analyze the composition of samples. The surface area of Bi_2WO_6 and Au/Bi_2WO_6 hybrid nanostructures with different Au loading were analyzed using Autosorb iQ surface area analyzer and AsiQwin software. Electron spin resonance (ESR) measurements were carried out using a Bruker ER200-SRC spectrometer at ambient temperature. A 300W Xe lamp equipped with the 400nm cutoff filter was used the irradiation source in ESR studies. All the ESR measurements were carried out using the following settings: 20 mW microwave power, 100 G scan range and 1 G field modulation. The photocurrent measurement, electrochemical impedance spectroscopy (EIS) measurement, and Mott-Schottky experiment were carried out in a standard three-electrode cell containing 0.5 mol/L Na_2SO_4 aqueous solution with a platinum foil and a saturated calomel electrode as the counter electrode and the reference electrode, respectively, on a CHI 760D workstation (Shanghai, China). The working electrode was prepared as described in the recent reports.[32] A 300 W Xe lamp with a 400nm cutoff filter was chosen as a visible light source. All of the electrochemical measurements were performed at room temperature.

2.4 Photocatalytic activity

Photocatalytic selective oxidation of benzyl alcohol was conducted in a 25 ml round-bottomed transparent glass flask equipped with a sealed spigot. Typically, the catalyst (50 mg) and benzyl alcohol (0.35 mmol) were added into the solvent of ultrapure water (5ml). This system was stirred for 30 min in dark to achieve adsorption equilibrium of reagents. The suspensions were irradiated under ambient conditions: i.e., room temperature and atmospheric pressure. A 300W Xe lamp (PLS-SXE 300, Beijing Perfect, Co. Ltd.) with 400nm cutoff filter was employed as the irradiation source. The reaction under light irradiation was maintained at the same temperature as that in dark to ensure the comparison was meaningful. Aliquots (1.0 ml) were collected at given time intervals and filtered through a Millipore filter (pore size 0.45μm) to remove the catalyst particles. The filtrates were analyzed by using an Agilent high performance liquid chromatograph (1200 HPLC) equipped with a diode-array detector (G1315C) and C18 column. The mobile phase was a mixture of 70% acetonitrile and 30% ultrapure water. Conversion of alcohol and selectivity of aldehyde or acid were calculated as

RSC Advances Accepted Manuscript

$$\text{Conversion (\%)} = [(C_0 - C_{\text{alcohol}}) / C_0] \times 100$$

$$\text{Selectivity (\%)} = [C_{\text{aldehyde}} \text{ or } C_{\text{acid}} / (C_0 - C_{\text{alcohol}})] \times 100$$

Where C_0 was the initial concentration of alcohol, C_{alcohol}, C_{aldehyde} and C_{acid} were the concentration of the substrate alcohol and the corresponding aldehyde or acid at a certain time after the reaction, respectively.

As to photocatalytic reduction of Cr(VI), 50 mg photocatalysts were dispersed into 50 mL Cr(VI) solution (20 mg/L), based on Cr in a dilute $K_2Cr_2O_7$ solution. The mixed suspension was stirred in the dark for 30min to establish the adsorption-desorption equilibrium and then exposed to visible light irradiation. During the process of the reaction, 3 mL of the suspension was collected at certain time intervals and centrifuged to remove the catalyst particles. The supernatant was analyzed on an UV-vis spectrophotometer and the normalized temporal concentration changes (C/C_0) of Cr(VI) were calculated on the basis of the change in the absorbance at ca. 371 nm.

3. Results and discussion

3.1 Phase structure, morphology and S_{BET}

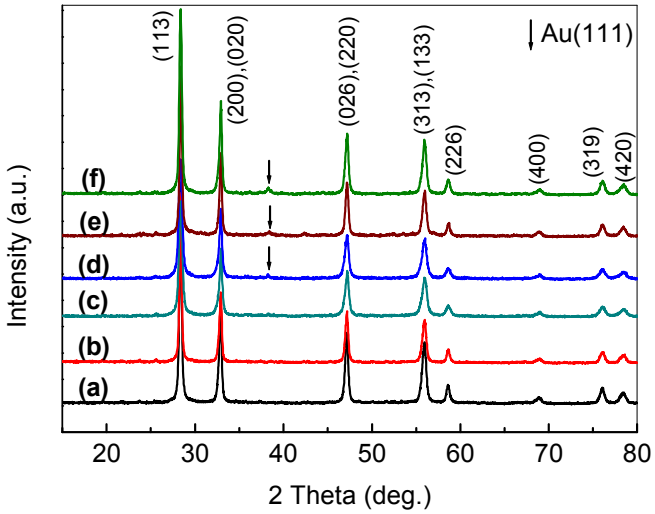

Fig. 1 XRD patterns of Au/Bi_2WO_6 hybrid nanostructures with different Au contents (wt%) (a) Bi_2WO_6, (b) 0.5% Au/Bi_2WO_6, (c) 1.0% Au/Bi_2WO_6, (d) 2.0% Au/Bi_2WO_6, (e) 3.0% Au/Bi_2WO_6, (f) 4.0% Au/Bi_2WO_6, respectively.

The crystal structure and phase composition of the as-prepared samples were investigated using XRD. Fig. 1 indicated the XRD patterns of Au/Bi_2WO_6 hybrid nanostructures with different Au contents. XRD data

RSC Advances Accepted Manuscript

revealed that the main phase of all the samples can be identified as the orthorhombic phase of Bi_2WO_6, which matched very well with the reported data (JCPDS no. 73-1126).[33] In detail, as shown in Fig.1, the main diffraction peaks at 2θ of 28.3°, 32.8°, 47.1°, 55.8°, and 58.5° corresponded to the indices of (113), (200), (020), (220), (026), (313), (133), and (226) planes, respectively. For the samples with higher Au contents (2.0-4.0wt% Au/Bi_2WO_6), weak peaks belonging to Au(111) diffraction were observed at 2θ~38°, indicating the presence of metallic Au.[34] However, the diffraction peaks could not be observed due to the weak signal beyond the XRD detection limit when the Au content was below 2.0%.

Fig. 2 displayed the TEM images of bare Bi_2WO_6 nanosheets and Au/Bi_2WO_6 hybrid nanostructures having different amounts of Au loading. It can be seen that bare Bi_2WO_6 sample had an irregular nanosheet morphology (Fig. 2a). As shown in the inset of Fig. 2a, selective area electron diffraction (SAED) pattern of individual nanosheets showed regular square diffraction spot array, which corresponded to the lattice spacing of 0.274, 0.272 and 0.381 nm from the (200), (020) and (220) Bragg reflection of orthorhombic Bi_2WO_6, respectively. During the reduction of Au^{3+} in the presence of Bi_2WO_6 nanosheets, the original light yellow suspension changed to dark gray indicating the formation of Au/Bi_2WO_6. TEM images of Fig. 2b-2d clearly showed the uniform dark dots distributed homogeneously on the surface of Bi_2WO_6 nanosheets after Au deposition. Further HRTEM observation (Fig. 2e) indicated that the distances between the adjacent lattice fringes were about 0.381 nm and 0.274 nm, in agreement with the *d*-spacing of the (220) and (200) planes of orthorhombic Bi_2WO_6.[33,35] As for the sample of 2.0% Au/Bi_2WO_6, besides the lattice fringes corresponding to orthorhombic phase of Bi_2WO_6, another kind of lattice fringes with *d* spacing of 0.236 nm for the dark dots can be found in the HRTEM image (Fig. 2e), which can be indexed as the (111) plane of face-centered cubic Au (JCPDS No. 04-0784).[34] Therefore, the dark dots can be identified as Au NPs.

Au NPs were visible in TEM images even for 0.5wt% Au/Bi_2WO_6 sample (Fig. 2b). When the weight ratio of Au to Bi_2WO_6 increased, both the size and density of Au NPs gradually increased (Fig. 2c and 2d). We have calculated the size of Au NPs for the prepared nanostructures with different Au loading amounts and the size distribution was given in Fig. 2f. The average sizes of Au NPs were determined to be 3.2, 4.6 and 6.1 nm corresponding to Au/Bi_2WO_6 with different weight ratio of 0.5wt%, 2.0wt% and 4.0wt%, respectively. Some uneven distribution of Au NPs and slightly wider size distribution were observed at 4.0 wt% loading. Additionally, energy dispersive X-ray (EDX) analysis was conducted for element

RSC Advances Accepted Manuscript

constituents of the hybrid nanostructures, which were shown in Fig. S1A (see Electronic supplementary information, ESI). Au, Bi and W were found in the EDX spectrum of 3.0 wt% Au/Bi_2WO_6 sample. Quantitative results gave the atomic ratio of 2.15 for Bi/W, which was close to the ideal value of 2 considering the instrumental error. Assuming a complete reduction of $HAuCl_4$ to Au, the calculated Au/Bi_2WO_6 weight ratios were compared with the measured ratios (from EDX analysis, average of three measurements). A linear relationship with a slope of 0.76 was found (see Fig. S1B of ESI), which indicated that the weight percentage of Au deposited on Bi_2WO_6 was proportional to the amount of $HAuCl_4$ in the reaction mixture. Because the slope for the linear relationship was less than 1, it was clear that not all of $HAuCl_4$ was reduced and deposited onto Bi_2WO_6 as Au NPs. Overall, these results demonstrated that loading of Au on Bi_2WO_6 nanosheets can be controlled simply by changing the adding ratio of reactants.

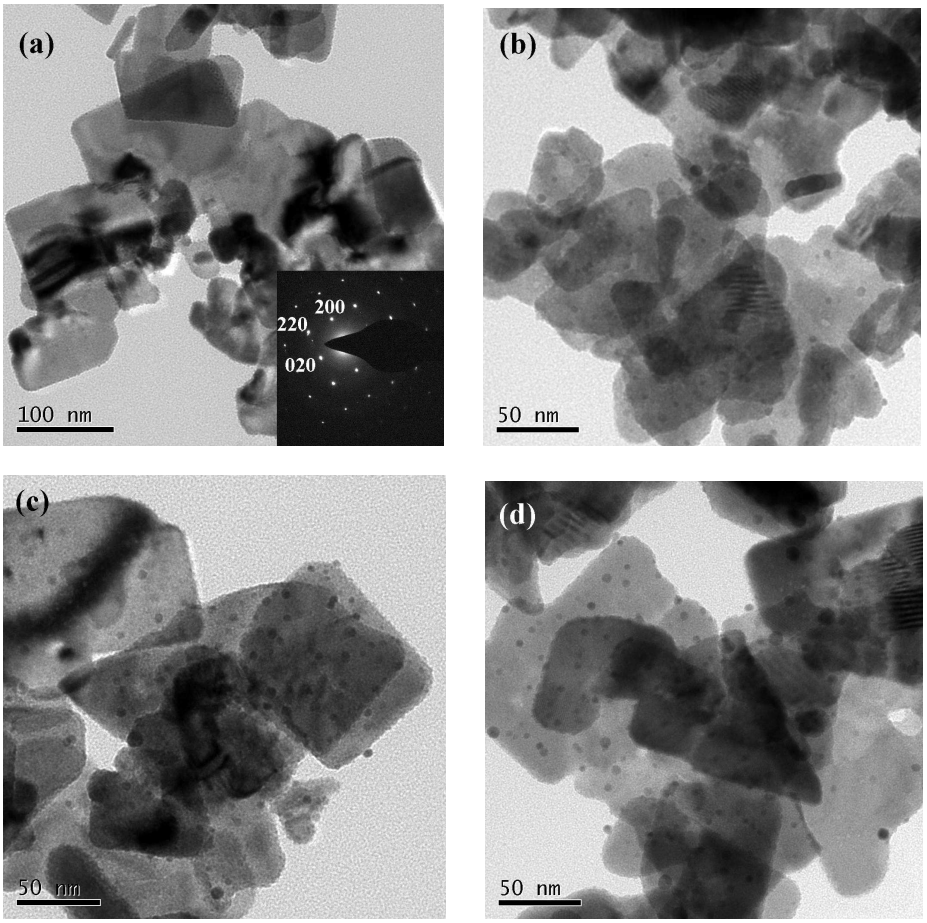

RSC Advances Accepted Manuscript

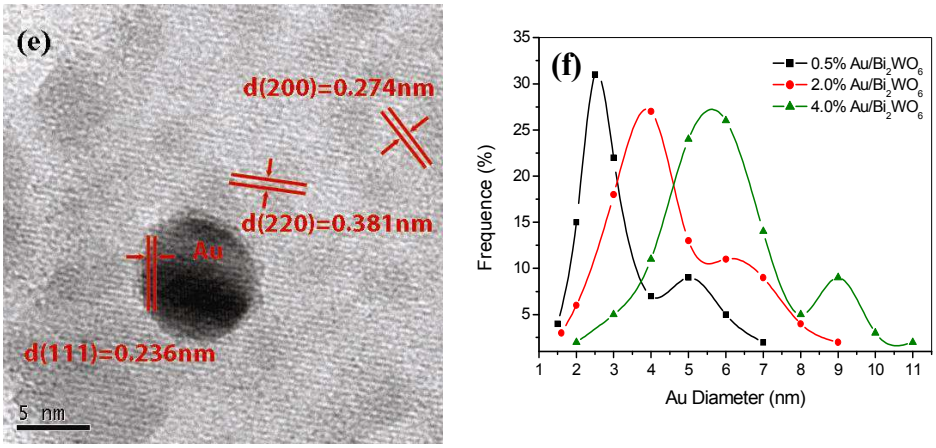

Fig. 2 TEM images of bare Bi_2WO_6 nanosheets (a) and Au/Bi_2WO_6 nanocomposites formed at different Au/Bi_2WO_6 weight ratios of 0.5% (b), 2.0% (c), and 4.0% (d). (e) HRTEM image for the sample from panel c; (f) the size distribution of Au NPs on Bi_2WO_6 nanosheets.

Besides, the specific surface areas (S_{BET}) for pristine Bi_2WO_6, Au/Bi_2WO_6 hybrid nanostructures with different Au/Bi_2WO_6 weight ratios of 0.5%, 1.0%, 2.0%, 3.0%, and 4.0%, were determined to be 29.66, 27.94, 25.99, 24.10, 22.54, and 20.38 m^2/g, respectively. The pristine Bi_2WO_6 nanosheets had a relatively high S_{BET} up to 29.66 m^2/g, while the S_{BET} of Au/Bi_2WO_6 samples slightly decreased with increasing Au contents after Au NPs deposition. The decrease of S_{BET} is because the specific surface area (m^2/g) is expressed per gram of the samples. The density of Au (19.3 g/cm^3) is more than that of Bi_2WO_6. Consequently, the densities of Au/Bi_2WO_6 samples increased with increasing Au amount, resulting in the reduction of S_{BET}.[34]

3.2. Chemical state and optical properties

Further evidence for the chemical composition and oxidation states of the as-prepared 2.0wt% Au/Bi_2WO_6 hybrid nanostructure was obtained by XPS analysis. The XPS spectra of 2.0wt% Au/Bi_2WO_6 were shown in Fig. 3A-D. It can be seen that the sample contained only Bi, W, O and Au elements and a trace amount of carbon. The C element was ascribed to the residual carbon from the precursor solution and the adventitious carbon from the XPS instrument itself. Fig. 3B-D showed the high-resolution spectra of the Au 4f, Bi 4f, and W 4f regions, respectively. The high-resolution XPS spectrum of Au 4f was presented in Fig. 3B. The Au 4f spectrum of 2.0wt% Au/Bi_2WO_6 was composed of two peaks at the binding energies of 83.8 and 87.5 eV, assigned to Au $4f_{7/2}$ and Au $4f_{5/2}$, respectively, suggesting that the Au species in the sample were presented

RSC Advances Accepted Manuscript

in the metallic state.[36] No oxidized gold species were detected. In Fig. 3C, it was obvious that the Bi 4f spectrum consisted of two peaks with binding energies around 158.7 and 164.0 eV, which corresponded to the signals from doublets of Bi $4f_{7/2}$ and Bi $4f_{5/2}$ in the trivalent oxidation state, and no other peaks of low oxidation state. As indicated in Fig. 3D, the peaks at 37.5 and 35.2 eV, corresponding to W $4f_{5/2}$ and W $4f_{7/2}$, respectively, can be assigned to a W^{6+} oxidation state.[33] Based on the XRD, HRTEM, and XPS results demonstrated above, we can conclude that the loaded Au should be metallic state Au NPs. Furthermore, the peak areas were determined for the quantitative elemental analysis of Bi, W, O and Au in 2.0wt% Au/Bi_2WO_6 hybrid nanostructure, and the atomic ratio of Bi: W: O: Au was 2.1: 1: 6.08: 0.08. Converted to the weight ratio of Au and Bi_2WO_6, about 1.69 wt% of Au NPs were deposited on the Bi_2WO_6 nanosheets, which was close to the measured value of EDX analysis (1.50 wt%).

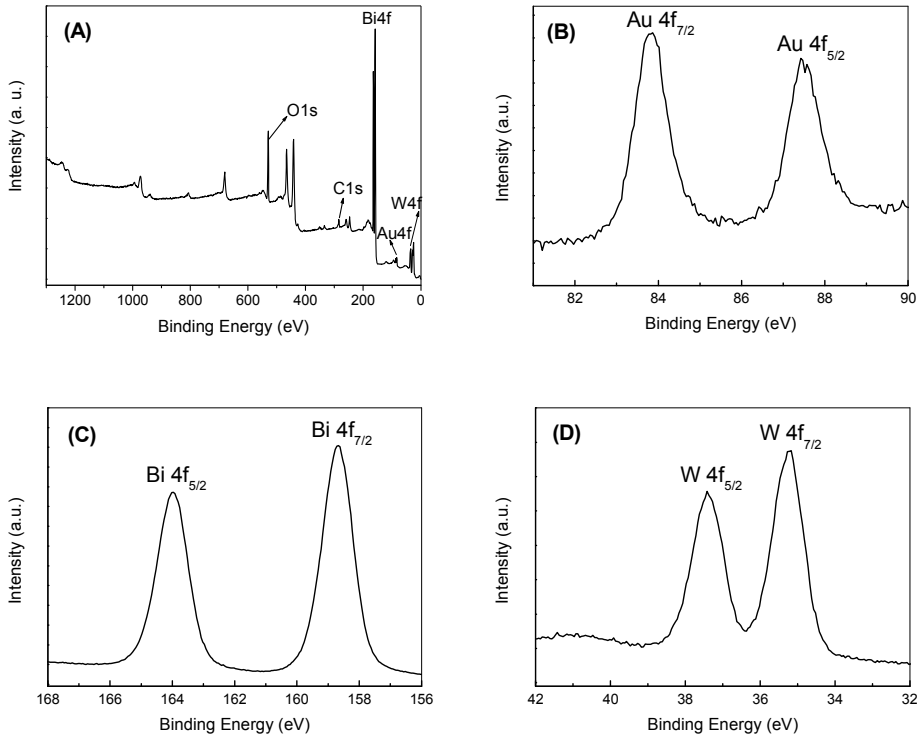

Fig. 3 XPS spectra of 2.0wt% Au/Bi_2WO_6 sample. (A) the survey spectra, and the high resolution XPS spectra of the sample, (B) Au 4f, (C) Bi4f, and (D) W4f.

The UV-Vis diffuse absorption spectra of bare Bi_2WO_6 and Au/Bi_2WO_6 hybrid nanostructures with different Au contents were presented in Fig. 4. Bare Bi_2WO_6 nanosheets exhibited photo-absorption from UV light region to visible light at about 470 nm, due to the intrinsic band-gap transition. The band gap

RSC Advances Accepted Manuscript

energy (E_g) was calculated based on the absorption spectra by the formula,[37] $(\alpha h\nu)^{1/n} = A(h\nu - E_g)$, where h is Planck's constant, ν is frequency of vibration, α is the absorption coefficient, E_g is the band gap, and A is a proportionality constant. The value of the exponent n denotes the nature of the sample transition and n = 0.5 when assuming a direct allowed transition. According to the results of this analysis, the band gap values of bare Bi_2WO_6, 1.0% Au/Bi_2WO_6, 2.0% Au/Bi_2WO_6, and 4.0% Au/Bi_2WO_6 samples were 2.76, 2.74, 2.72, and 2.71eV, respectively. The Au/Bi_2WO_6 nanocomposites exhibited the similar E_g to pristine Bi_2WO_6, which demonstrated that the introducing of Au had almost no influence on the band gap energy of Bi_2WO_6. However, the absorption spectra of Au/Bi_2WO_6 samples were obviously different from that of pure Bi_2WO_6. After Au loading, the nanocomposite samples exhibited a peak shoulder centered at ca. 580 nm for 1.0% and 2.0% Au/Bi_2WO_6, which was due to the absorption of the Au surface plasmon resonance (SPR). The surface plasmon absorption in the metal NPs arises from the collective oscillations of the free conduction band electrons that are enhanced by the incident electromagnetic radiation.[38] For 4.0% Au/Bi_2WO_6, the SPR absorption peaks shifted from 580 to 589 nm. Moreover, the intensity of the SPR band initially increased with increasing of Au loading amount up to 2.0%, but then decreased for the sample of 4.0% Au/Bi_2WO_6. It has been reported that the band position and intensity of the plasmon absorption strongly depend on the Au content, particle size of Au NPs, and the surrounding environment.[38] The shifting of SPR absorption peaks in Fig. 4 was probably ascribed to the increase in the particle sizes of Au for 4.0% Au/Bi_2WO_6, as partially evidenced by the TEM images shown in Fig. 2.

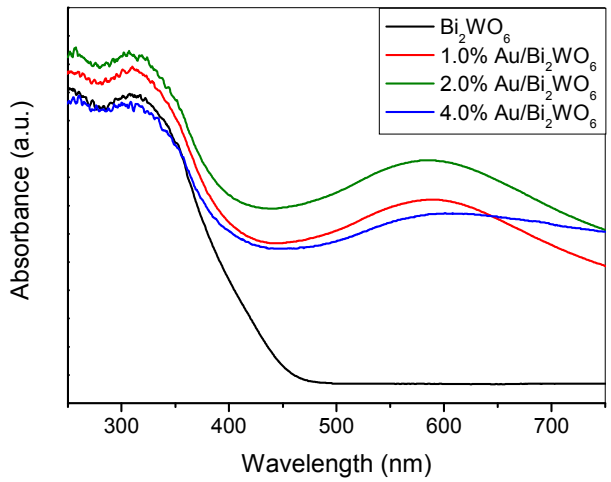

Fig. 4 UV-Vis absorbance spectra of bare Bi_2WO_6 nanosheets and Au/Bi_2WO_6 hybrid nanostructures (1%, 2% and 4% Au/Bi_2WO_6).

RSC Advances Accepted Manuscript

3.3. Photocatalytic selective oxidation of benzyl alcohol

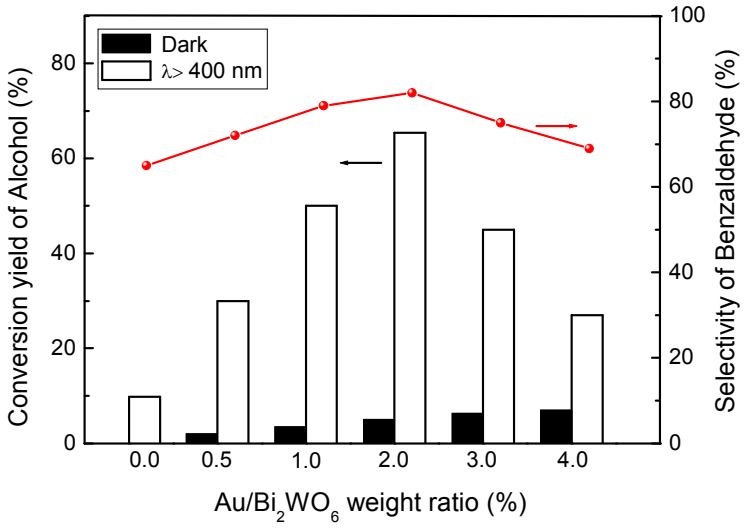

Fig. 5 The conversion yield of benzyl alcohol and the selectivity to benzaldehyde over different Au/Bi_2WO_6 nanocomposite catalysts. Reaction conditions: catalyst (50 mg), benzyl alcohol (0.35 mmol), solvent water (5 mL), air atmosphere, reaction time 8h, and temperature 298±1K.

Photocatalytic activity of the as-prepared Au/Bi_2WO_6 hybrid nanostructures was investigated by the selective oxidation of benzyl alcohol in water, often used as a substrate for the aerobic oxidation.[28,36] Fig. 5 summarized the results of benzyl alcohol oxidation after 8h reaction in the dark (black bars) or under visible light irradiation (λ>400nm, white bars). With bare Bi_2WO_6, no reaction occurred in the dark, and 9.8% benzyl alcohol was oxidized under visible light irradiation. In contrast, Au/Bi_2WO_6 catalysts in the dark exhibited certain activity to selective oxidation of benzyl alcohol. It was consistent with the previous reports, in which small Au particles (diameter < 5nm) were active for the aerobic oxidation in the dark.[39,40] Noticeably, the loading of an appropriate amount of Au NPs can effectively enhance the photoactivity of the nanocomposites as compared to that of blank Bi_2WO_6 and the selectivity distribution of the product was changed accordingly. As shown in Fig. 5, when the weight addition ratio of Au was 2.0%, optimal photocatalytic performance was obtained. Under 8h visible light irradiation, the conversion of benzyl alcohol and the selectivity for benzaldehyde over 2.0% Au/Bi_2WO_6 were measured to be ca. 65.4% and ca. 82%, which were higher than the values obtained over blank Bi_2WO_6 (ca. 9.8% conversion and 65%

RSC Advances Accepted Manuscript

selectivity for benzaldehyde). Specifically, the carbon mass balance estimation based on HPLC analysis confirmed that the primary products of photocatalytic oxidation of benzyl alcohol were aldehyde and acid within the scope of intrinsic error from a HPLC analysis. Thus, the main by-product was benzoic acid instead of carbon dioxide in the present experimental conditions. However, further increasing the Au content (>2.0%) led to a distinct decrease in the conversion of benzyl alcohol possibly due to the increase of opacity and light scattering of samples, which actually reduced the effective irradiation absorbed by the reaction suspension solution.[34] On the other hand, excessive Au NPs may block the surface active sites and thus hinder the photocatalytic selective oxidation.[41] Additionally, to demonstrate the general applicability of Au/Bi_2WO_6 photocatalyts, we have further tested their visible light photoactivity toward selective oxidation of a range of benzylic alcohols with different substituted groups, and the results were listed in Table S1 (see ESI). It was clear to see that 2.0% Au/Bi_2WO_6 was also highly active for the oxidation of these benzylic alcohols to the corresponding aldehydes with good selectivity.

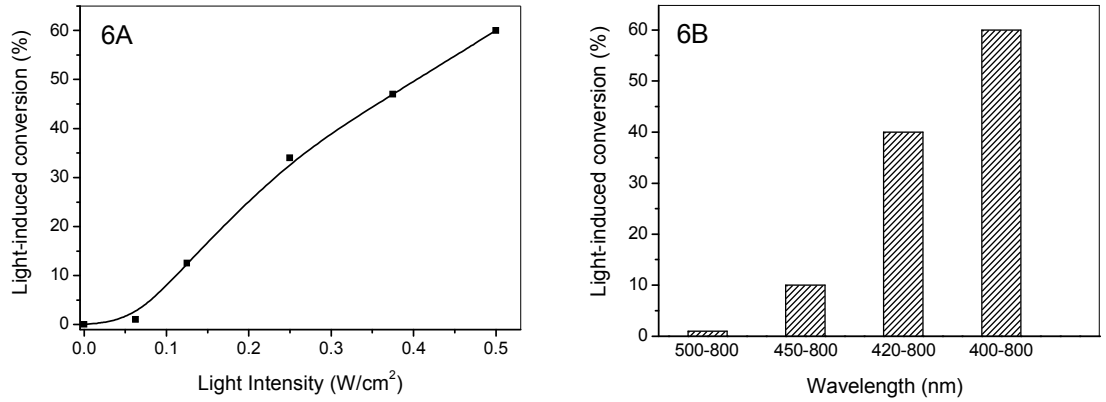

Fig. 6 The effect of the light intensity **(A)** and the range of light wavelength **(B)** on the photo-oxidation of benzyl alcohol. Reaction conditions: 2.0% Au/Bi_2WO_6 catalyst (50 mg), benzyl alcohol (0.35 mmol), solvent water (5 mL), air atmosphere, reaction time 8 h, and temperature 298±1K.

To better understand the enhancement mechanism of photocatalytic performance over Au/Bi_2WO_6 samples, the effects of light intensity and wavelength range on the photoactivity were investigated. The light-induced conversion of benzyl alcohol was calculated by subtracting the conversion yield of the reaction in the dark from that of the irradiated system. As indicated in Fig. 6A, the light-induced conversion of benzyl alcohol on 2.0% Au/Bi_2WO_6 catalyst was proportional to the intensity of visible light. The results clearly show that higher light intensities give rise to greater light-induced conversion of benzyl alcohol,

RSC Advances Accepted Manuscript

which reveals that incident light intensity plays an important role in the present photocatalytic system. Under visible light irradiation, stronger light intensities excited more Au/Bi_2WO_6 and generated more active species, resulting in a higher conversion rate. Similar linear dependence of reactant conversion with light intensity was also observed in the recent reports.[42,43] The range of wavelength also had influence on the photo-oxidation process. When the reaction system was illuminated with different ranges of light wavelength (Fig. 6B), such as 400-800, 420-800, and 450-800 nm, while keeping other experimental conditions identical, the conversions of benzyl alcohol declined gradually. However, as depicted in Fig. 6B, almost no alcohol was oxidized with the illumination of light wavelength 500-800 nm, although a strong plasmonic absorption occurs in this range (Fig. 4). The result implied that there was no direct relationship between the SPR intensity and the photocatalytic activity of oxidation alcohol.

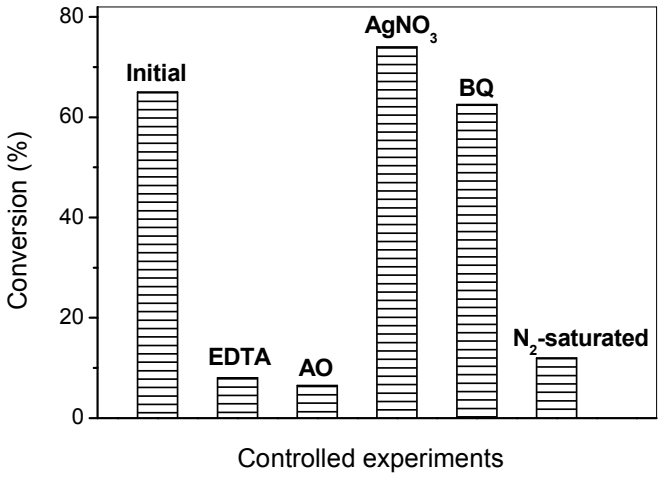

Fig. 7 Controlled experiments of photocatalytic selective oxidation of benzyl alcohol in the presence of various scavengers or in the absence of O_2 over 2.0% Au/Bi_2WO_6 catalyst in water under visible light irradiation for 8 h.

Herein, the underlying reaction mechanism involved for the photocatalytic oxidation of benzyl alcohol in water over Au/Bi_2WO_6 was investigated in detail. First, the controlled experiments in the absence of molecule oxygen (O_2) or with adding various scavengers were examined under visible light illumination. When disodium ethylenediaminetetraacetate (EDTA) or ammonium oxalate (AO) was added to the benzyl alcohol system to trap the holes,[44,45] the conversion rate of benzyl alcohol decreased significantly (Fig. 7), revealing that the photogenerated holes are major oxidative species for the selective oxidation of benzyl

RSC Advances Accepted Manuscript

alcohol. The addition of electron scavenger $AgNO_3$ could increase the conversion of benzyl alcohol (Fig. 7)[46], further confirming that the photogenerated holes were crucial for the oxidation of benzyl alcohol. Controlled experiment in the inert N_2 atmosphere showed low conversion of benzyl alcohol, suggesting that oxygen played an important role in photocatalytic oxidation of benzyl alcohol. However, when benzoquinone (BQ), a scavenger for superoxide radicals ($O_2^{\cdot-}$), was added into the reaction system, the conversion of benzyl alcohol was almost unchanged, indicating that superoxide radicals was not essential for the selective oxidation of benzyl alcohol over Au/Bi_2WO_6. Based on the above controlled experimental results, molecular oxygen might participate directly in the oxidation of benzyl alcohol, which was similar to the oxygen atom transfer mechanism in TiO_2 photocatalytic system.[47] On the other hand, the role of molecular oxygen could be the trapping photogenerated electrons to form surperoxide radicals, which could inhibit the recombination of photogenerated charge carriers and facilitate the selective oxidation of benzyl alcohol induced by the photo-holes.

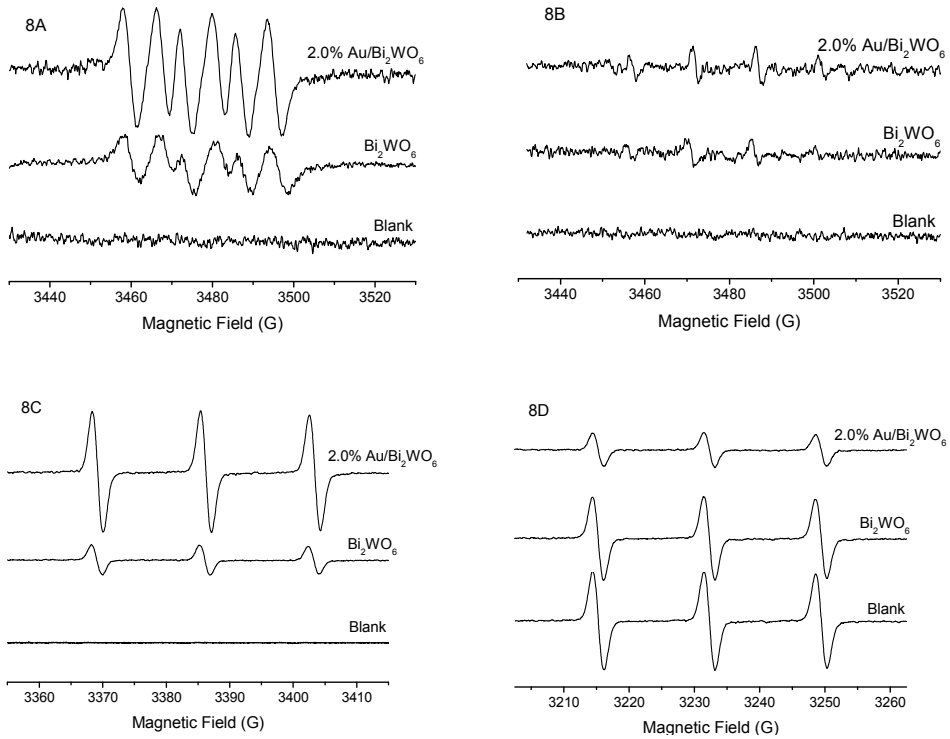

Fig. 8 Significant enhancement effect of Au NPs in Au/Bi_2WO_6 nanocomposites for generation of reactive oxygen species and charge carriers under visible light irradiation. ESR spectra obtained from samples containing different spin probes (**A:** 40 mM DMPO methanol solution; **B:** 40 mM DMPO aqueous solution; **C:** 0.04 mM CPH aqueous solution; **D:** 0.04 mM TEMPO aqueous solution) and 0.1 mg/mL

RSC Advances Accepted Manuscript

Bi_2WO_6 or 2.0% Au/Bi_2WO_6. All spectra were recorded after 6 min of visible light irradiation. The blank represents the sample containing spin probe alone under light illumination, and the sample containing spin probe and catalysts in dark.

To identify the generation of reactive species and further investigate the enhancing mechanism of photocatalytic performance by deposition Au NPs, ESR spectroscopy with spin trapping and labeling was chosen as an effective characterization technique. Here, we selected 5,5-dimethyl-1-pyrroline N-oxide (DMPO)[48] as a spin trap for the hydroxyl radicals and superoxide radicals, 2,2,6,6-tetramethylpiperidine-1-oxyl (TEMPO)[49] and 1-hydroxy-3-carboxy-2,2,5,5-tetramethylpyrrolidine (CPH)[50] for the characterization of photogenerated electrons and holes. Fig. 8 showed the ESR spectra obtained from the solutions containing various spin probes and Bi_2WO_6 or Au/Bi_2WO_6 before and during the irradiation with visible light. As indicated in Fig. 8A, upon irradiation for 6 min in the presence of Bi_2WO_6, we clearly observed the characteristic spectrum for the adduct DMPO/·OOH formed between DMPO and superoxide radicals.[46] When 2.0% Au/Bi_2WO_6 hybrid nanostructure was added, the signal intensity of DMPO/·OOH increased obviously (about 3 times). These results indicated that the superoxide radicals were generated over bare Bi_2WO_6 or Au/Bi_2WO_6 under visible light illumination and loading of Au onto Bi_2WO_6 significantly enhanced the photogeneration of $O_2^{\cdot-}$. Besides, the intensity changes of ESR signals for DMPO/·OOH adducts as a function of irradiation time in 2.0% Au/Bi_2WO_6 dispersion were shown in Fig. S2 of ESI. It can be seen from Fig. S2 that the amount of DMPO/·OOH adducts exhibited the gradual increase in the first 6 min of irradiation, and then reached a stable state in 8 min.

Meanwhile, it can be seen from Fig. 8B that weak signals of DMPO/·OH adduct were observed in pure Bi_2WO_6 and 2.0% Au/Bi_2WO_6 suspension solutions under visible light irradiation. To clarify the formation path of ·OH, we have performed the Mott-Schottky plot for Bi_2WO_6 nanosheets, as shown in Fig. S3 (see the ESI). The flat-band potential of Bi_2WO_6, as calculated from the *X* intercepts of the linear region, was found to be -0.44 V *vs* Saturated Calomel Electrode, SCE (equivalent to -0.20 V *vs* normal hydrogen electrode, NHE). It is known that the bottom of the conduction bands was more negative by ~ -0.1 V than the flat band potential for many n-type semiconductors.[51] Therefore, the estimated positions of conduction and valence bands of Bi_2WO_6 nanosheets were -0.30 and 2.46 V *vs* NHE respectively, based on the UV-vis diffuse reflectance spectrum of Bi_2WO_6 (Fig. 4). The redox potential for dissolved oxygen/superoxide

RSC Advances Accepted Manuscript

couple is -0.16 V and for the $H_2O/{\cdot}OH$ couple is 2.42 V *vs* NHE at pH 7.[52] The observed weak ·OH radicals in Fig. 8B may be attributed to very small difference (0.04 V) between the valence band edge of Bi_2WO_6 and the redox potential of $H_2O/{\cdot}OH$ couple. Besides, it could not be excluded that ·OH radicals were generated via the facile disproportionation of $O_2^{\cdot-}$ in water ($e^- + O_2^{\cdot-} + 2H^+ \rightarrow H_2O_2$) and the following H_2O_2 decomposition ($H_2O_2 + e^- \rightarrow {\cdot}OH + OH^-$).

CPH, though ESR silent itself, can be oxidized to form CP-nitroxide (CP·) radicals with a typical ESR spectrum of three lines with intensity ratios of 1:1:1. CPH is an often-used hole scavenger as it can be oxidized by holes.[48] Oxidation of CPH was accompanied by the enhancement of the ESR signals (Fig. 8C). Therefore, the generation of photoinduced holes and their behavior can be easily monitored by observing changes in the ESR spectrum of CPH. When CPH was exposed to visible light in the presence of Bi_2WO_6 or Au/Bi_2WO_6, we observed ESR spectra consisting of three-lines with hyperfine splitting constant of 16.2 G. More importantly, the ESR signal intensity generated from photoexcited 2.0% Au/Bi_2WO_6 was calculated as about 4 times the signal from bare Bi_2WO_6, indicating that deposition of Au on Bi_2WO_6 greatly enhanced the generation of photo-holes. The spin label TEMPO was used for identifying the photogenerated electrons in bare Bi_2WO_6 and 2.0% Au/Bi_2WO_6. TEMPO is a typical spin label molecule, having stable triplet ESR spectrum. It can be reduced by electrons associated with photoexcited semiconductors, leading to a hydroxyl amine (TEMPOH) which lacks an ESR signal.[47] As shown in Fig. 8D, the ESR spectrum of an aqueous solution of TEMPO showed a stable signal having three peaks with intensity of 1:1:1. The signal intensity decreased moderately within 6 min of irradiation in the presence of Bi_2WO_6; however, a considerable reduction of ESR signal was observed during the irradiation of 2.0% Au/Bi_2WO_6 nanocomposites. These results demonstrated that the electrons were produced from the photoexcited Bi_2WO_6 or Au/Bi_2WO_6, and loading of Au onto Bi_2WO_6 can greatly enhance the reactivity of photoinduced electrons. This may be attributable to the low Fermi level of Au, resulting in the transfer of conduction band electrons from Bi_2WO_6 to Au NPs and the increased availability of photoelectrons for the reduction.

The ESR results in Fig. 8 displayed the deposition of Au NPs onto Bi_2WO_6 nanosheets can significantly enhance the photo-induced generation of the identified active species. As mentioned above, the loading amount of Au NPs played an important role in the photocatalytic activity of Bi_2WO_6. Therefore, it was critical to investigate whether the amount of Au loading had similar effects on the photogeneration of active

RSC Advances Accepted Manuscript

species. The effects of Au loading on the enhancement of photoholes, superoxide radicals, and photoelectrons were depicted in Fig. 9. A similar dependence on Au loading was observed for superoxide radicals and photoelectrons. An initial increase in the ESR signal intensity was noted for Au/Bi_2WO_6 nanocomposites with weight ratio of Au up to 1.0%. Diminishing ESR signal intensities were observed for nanocomposites having a higher weight ratio of Au. For CPH, which was used to determine photo-oxidative behavior caused by holes, a different trend was noticed. As indicated in Fig. 9, the ESR signal of CP· increased initially with increasing Au weight ratio up to 2.0%. Importantly, it is of interest to note that the ESR signal obtained for CPH and the photocatalytic activity of alcohol oxidation had a similar dependence on the amounts of Au loading. This correlation implied a mechanistic connection between the photogeneration of holes and the photocatalytic performance. The results also demonstrated that photogenerated holes, rather than superoxide radicals and photoelectrons, played more dominant role in the selective oxidation of benzylic alcohols by Au/Bi_2WO_6, consistent with the results of active species trapping experiments.

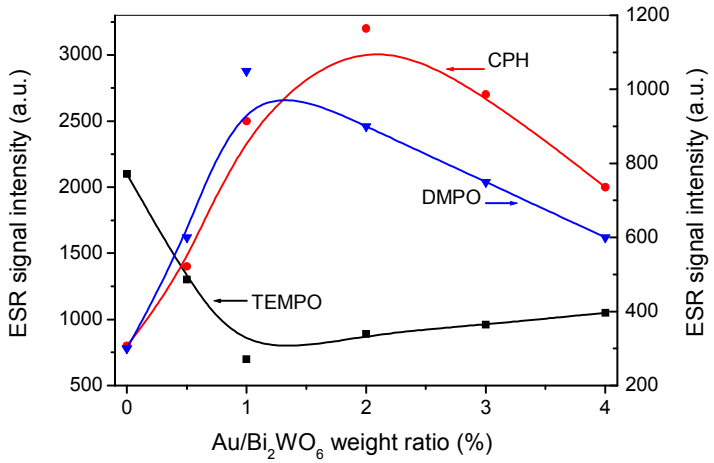

Fig. 9 Effect of Au loading amount on the enhancement of photoinduced generation of photoholes, superoxide radicals, and photoelectrons.

3.4. Photocatalytic reduction of Cr(VI)

Carcinogenic Cr(VI) ion is a common byproduct in industries of electroplating, tanning, and dying. The effective removal of toxic Cr(VI) ions would benefit the environment remediation, but very limited methods have been developed to eliminate such toxic ions at the current time. The significant enhancement of photocatalytic activity resulted from the loading Au NPs on Bi_2WO_6 nanosheets can also be verified by

RSC Advances Accepted Manuscript

photocatalytic reduction of toxic heavy metal ions Cr(VI). Fig. 10 represented the normalized concentration (C/C_0) of Cr(VI) calculated at different time interval. Obviously, Au/Bi_2WO_6 nanocomposites and blank Bi_2WO_6 were visible light photoactive for the reduction of Cr(VI) in water. Similar to the case of selective oxidation of alcohols, a proper loading of Au NPs can effectively promote the reduction process in comparison with blank Bi_2WO_6, but excessive Au loading (>1.0 wt%) in the nanocomposites resulted in a distinct decrease in the photoactivity due to the decreased amount of primary photoactive ingredient Bi_2WO_6 and the lower light intensity through the depth of reaction solution. Interestingly, the generation of photoelectrons determined by using TEMPO as ESR spin label and the photocatalytic activity of Cr(VI) reduction had a similar variation tendency with the amounts of Au loading. The results suggested that the generation and activity of photogenerated electrons in 1.0% Au/Bi_2WO_6 would be more efficient than other Au/Bi_2WO_6 nanocomposites, which contributed to improving the photocatalytic activity of Cr(VI) reduction. Additionally, the stability and recyclability of photocatalysts are extremely important for practical applications. The cycling runs for the photo-reduction of Cr(VI) with the optimal nanocomposites 1.0% Au/Bi_2WO_6 were performed to evaluate its photocatalytic stability and recyclability. Fig. 11 illustrated the relationship between removal ratio of Cr(VI) and cycle times. After reusing five cycles, the photo-reduction rate of Cr(VI) still remains over 85%. In addition, XRD patterns of 1.0% Au/Bi_2WO_6 sample before and after reaction, as shown in Fig. S4 of ESI, distinctly revealed that the hybrid nanostructures of Au/Bi_2WO_6 were stable in the present experimental conditions.

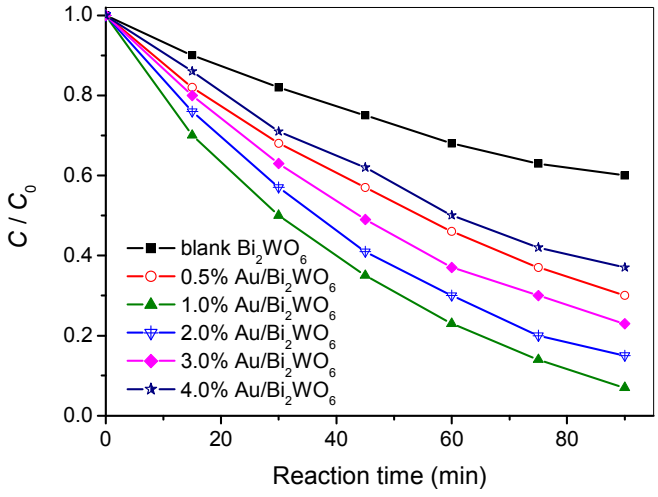

Fig. 10 Photocatalytic reduction of Cr(VI) in the blank Bi_2WO_6 and various Au/Bi_2WO_6 nanocomposite aqueous dispersions under visible light irradiation.

RSC Advances Accepted Manuscript

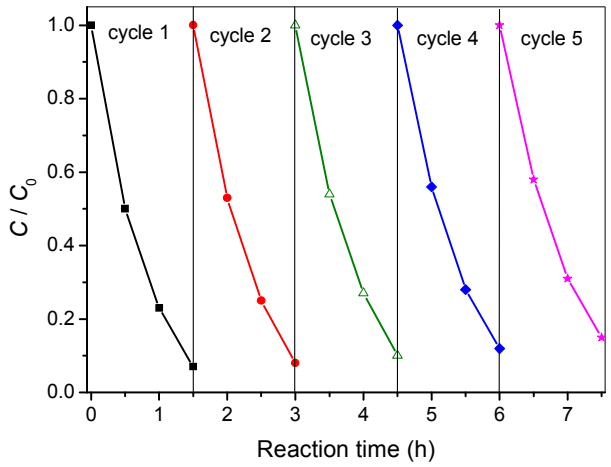

Fig. 11 Cycling runs for the photocatalytic reduction of Cr(VI) over 1.0% Au/Bi_2WO_6 hybrid nanostructure under visible light irradiation.

The above deduction was further authenticated by the photoelectrochemical characterizations, which are widely used to determine the formation and transfer of photogenerated electrons from semiconductor under light illumination. As shown in Fig. 12A, the deposition of Au NPs generated the significant enhanced photocurrent under visible light irradiation, and more Au NPs were deleterious to the transient photocurrent. It is important to note that 1.0% Au/Bi_2WO_6 exhibited a larger photocurrent than bare Bi_2WO_6 and 2.0% Au/Bi_2WO_6, in line with the photocatalytic reduction of Cr(VI). The obvious increase in the transient photocurrent was mainly due to two aspects: i) the predominant plasmonic effect that increased the formation rate of electron-hole pairs over Bi_2WO_6; ii) the formation of Schottky barriers among Bi_2WO_6-Au-ITO glass, which led to the accelerated transfer of photogenerated electrons from Bi_2WO_6 to Au, and finally to ITO. We subsequently utilized the electrochemical impedance spectra (EIS) experiments to investigate the electron generation and the charge transport characteristics of bare Bi_2WO_6 and 1.0% Au/Bi_2WO_6. Generally, the interface charge separation efficiency can be examined by the EIS Nyquist plots. Fig. 12B showed the EIS Nyquist plots of Bi_2WO_6 and 1.0% Au/Bi_2WO_6 electrodes under dark and visible light irradiation. The smaller diameter of the arc radius on the EIS Nyquist plot of 1.0% Au/Bi_2WO_6 compared to that of Bi_2WO_6 under visible light irradiation revealed more effective separation of photogenerated electron-hole pairs and faster interfacial charge transfer induced by Au loading (Fig.12B),

RSC Advances Accepted Manuscript

which contributed to higher photo-activity of Cr(VI) reduction.

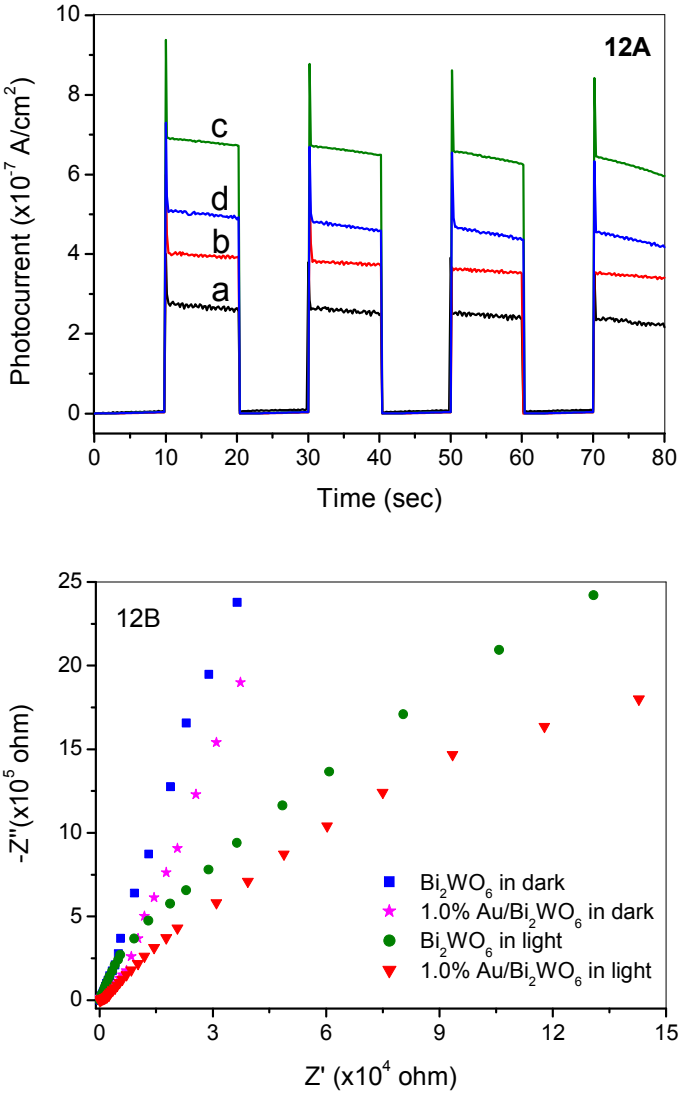

Fig. 12 (A) Transient photocurrent response of bare Bi_2WO_6 (a), 0.5% Au/Bi_2WO_6 (b), 1.0% Au/Bi_2WO_6 (c), and 2.0% Au/Bi_2WO_6 (d) nanocomposites under visible light irradiation; (B) EIS Nyquist plots of Bi_2WO_6 and 1.0% Au/Bi_2WO_6 nanocomposites in the dark and under visible light illumination in 0.5M Na_2SO_4 aqueous solution.

To further reveal the roles of loaded Au NPs for Cr(VI) reduction, the dependence of Cr(VI) removal on light wavelength range was investigated over 1.0% Au/Bi_2WO_6 nanocomposites and the results were presented in Fig. S5 of ESI. Clearly, a similar dependence on the light wavelength range was observed for

RSC Advances Accepted Manuscript

both alcohol oxidation and Cr(VI) reduction (Fig. 6B and Fig. S5). The results suggest that there is no direct relationship between the SPR intensity and the photocatalytic activity, which leads to a hypothesis that only plasmonic absorption is unable to create "chemically useful" energetic charge carriers in the Au/Bi_2WO_6 hybrid nanostructures for both selective oxidation of alcohols and photocatalytic reduction of Cr(VI).

According to the references, the Fermi level of Au NPs positions at ca. +0.45 V *vs* NHE.[53] Under the irradiation of 580 nm visible light ($h\nu$~2.15 eV), the SPR of Au NPs will be induced. Thus, the energy position of the SPR state for the Au NPs is about -1.70 eV *vs* NHE. Therefore, the excited energetic electrons in the SPR state can be injected into the conduction band of Bi_2WO_6 and the transfer process of energetic plasmonic electron is feasible thermodynamically. However, based on the dependence of the photocatalytic activity on the light wavelength for both alcohol oxidation and Cr(VI) reduction (Fig. 6B and Fig. S5), the enhancing effect by deposition Au NPs should be limited by simply SPR-mediated electron injection. A pivotal contributor, localized electromagnetic field formed by the SPR of loaded Au NPs, can't be ignored for the significantly improved photocatalytic performance in the present system (Scheme I). It has already proved to be able to increase the formation rate of electron-hole pairs of the semiconductor by a few orders of magnitude.[10,54] On the other hand, considering the lower Fermi level of Au NPs (+0.45 V *vs* NHE) with respect to the conduction band of Bi_2WO_6 (-0.30 V *vs* NHE), the photogenerated electrons in the conduction band of Bi_2WO_6 can be readily transferred to Au NPs, which could effectively separate the photogenerated carriers and finally result in the enhancement of photocatalytic activity.

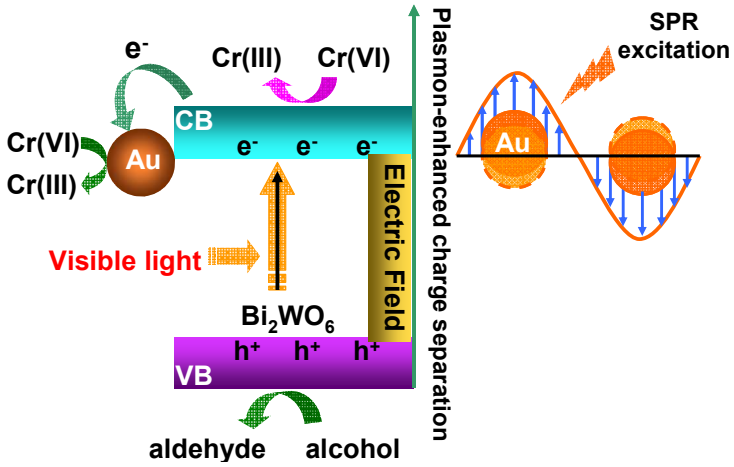

Scheme I Schematic diagram showing the photocatalytic process for the selective oxidation of benzylic

RSC Advances Accepted Manuscript

alcohol and reduction of Cr(VI) on the Au/Bi_2WO_6 nanocomposites.

4. Conclusions

In summary, we have reported that Au/Bi_2WO_6 hybrid nanostructures, fabricated via a simple hydrothermal approach combined with a rapid reduction-deposition method, can serve as visible-light selective photocatalysts in the green solvent water. Deposition Au NPs onto Bi_2WO_6 can greatly improve the photocatalytic performance of Bi_2WO_6 for both selective alcohol oxidation and Cr(VI) reduction. The optimal hybrid nanostructures for benzyl alcohol oxidation and Cr(VI) reduction were determined to be 2.0 wt% and 1.0 wt% Au/Bi_2WO_6 under visible light irradiation, respectively. To investigate the enhanced mechanism of loading Au, ESR with spin trapping and spin labeling, photocurrent, and EIS measurements were carried out to determine the photoinduced generation of active radicals, electron/hole pairs, and transport characteristics of photoelectrons for bare Bi_2WO_6 and Au/Bi_2WO_6. It was found that Au/Bi_2WO_6 exhibited the enhanced generation of reactive radicals and charge carriers when excited with visible light. Additionally, the enhanced generation of charge carriers and photocatalytic performance of alcohol oxidation or Cr(VI) reduction over Au/Bi_2WO_6 hybrid nanostructures showed a distinctive Au/Bi_2WO_6 ratio dependence. This enhancement effect may be attributed to the increase in the formation rate of electron-hole pairs of Bi_2WO_6 induced by SPR of Au NPs and higher efficiency of electron transfer due to the energy barrier between the conduction band of Bi_2WO_6 and Fermi energy of Au NPs. It is hoped that this work provides an effective way to improve the photocatalytic activity of semiconductors by incorporation of metal NPs with SPR effect, especially in the field of selective redox processes in water under the framework of green chemistry.

Acknowledgements

This work was supported by the National Natural Science Foundation of China (21307027, 51074067) and the Foundation of Henan Educational Committee (2010B150009).

Notes and references

Institute of Applied Chemistry, Henan Polytechnic University, Jiaozuo, 454003, P.R. China

Fax: +86-391-3987811; Tel: +86-391-3987818;

Email: yangjuanhpu@yahoo.com, daijun@hpu.edu.cn

RSC Advances Accepted Manuscript

† Electronic Supplementary Information (ESI) available: [EDX analysis of Au/Bi_2WO_6; the results of selective oxidation of various benzylic alcohols; ESR spectra of superoxide radicals; Mott-Schottky plot of Bi_2WO_6 nanosheets; XRD patterns of fresh and used 1.0% Au/Bi_2WO_6; the influence of light intensity and wavelength range on the photoreduction of Cr(VI)]. See DOI: 10.1039/xxxxxxxx/

1. A. Hagfeldt and M. Gratzel, *Chem. Rev.*, 1995, **95**, 49-68.
2. Z. G. Zou, J. H. Ye, K. Sayama and H. Arakawa, *Nature*, 2001, **414**, 625-627.
3. W. Morales, M. Cason, O. Aina, N. R. Tacconi and K. Rajeshwar, *J. Am. Chem. Soc.*, 2008, **130**, 6318-6319.
4. J. Zhang, Y. Wu, M. Xing, S. A. K. Leghai and S. Sajjad, *Ener. Environ. Sci.*, 2010, **3**, 715-726.
5. S. G. Kumar and L. G. Devi, *J. Phys. Chem. A*, 2011, **115**, 13211-13241.
6. J. Tian, Y. Sang, G. Yu, H. Jiang, X. Mu and H. Liu, *Adv. Mater.*, 2013, **25**, 5075-5080.
7. W. Zhou, H. Liu, J. Wang, D. Liu, G. Du and J. Cui, *ACS Appl. Mater. Interfaces*, 2010, **2**, 2385-2392.
8. Z. Zhang, J. Long, L. Yang, W. Chen, W. Dai, X. Fu and X. Wang, *Chem. Sci.*, 2011, **2**, 1826-1830.
9. J. Yang, D. Wang, H. Han and C. Li, *Acc. Chem. Res.*, 2013, **46**, 1900-1909.
10. D. Tsukamoto, Y. Shiraishi, Y. Sugano, S. Ichikawa, S. Tanaka and T. Hirai, *J. Am. Chem. Soc.*, 2012, **134**, 6309-6315.
11. S. Zhu, S. Liang, Q. Gu, L. Xie, J. Wang, Z. Ding and P. Liu, *Appl. Catal. B: Environ.*, 2012, **119-120**, 146-155.
12. W. Hou, W. H. Hung, P. Pavaskar, A. Goeppert, M. Aykol and S. B. Cronin, *ACS Catal.*, 2011, **1**, 929-936.
13. Y. Tian and T. Tatsuma, *J. Am. Chem. Soc.*, 2005, **127**, 7632-7637.
14. K. Awazu, M. Fujimaki, C. Rockstuhl, J. Tominaga, H. Murakami, Y. Ohki, N. Yoshida and T. Watanabe, *J. Am. Chem. Soc.*, 2008, **130**, 1676-1680.
15. C. Zhang and Y. F. Zhu, *Chem. Mater.*, 2005, **17**, 3537-3545.
16. F. Amano, A. Yamakata, K. Nogami, M. Osawa and B. Ohtani, *J. Am. Chem. Soc.*, 2008, **130**, 17650-17651.
17. G. S. Li, D. Q. Zhang, J. C. Yu and M. K. Leung, *Environ. Sci. Technol.*, 2010, **44**, 4276-4281.
18. Z. J. Zhang, W. Z. Wang, M. Shang and W. Z. Yin, *J. Hazard. Mater.*, 2010, **177**, 1013-1018.

RSC Advances Accepted Manuscript

19. D. J. Wang, G. L. Xue, Y. Z. Zhen, F. Fu and D. S. Li, *J. Mater. Chem.*, 2012, **22**, 4751-4758.

20. J. Yang, J. Dai and J. T. Li, *Sci. Adv. Mater.*, 2013, **5**, 1013-1023.

21. C. Y. Sun, D. Zhao, C. C. Chen, W. H. Ma and J. C. Zhao, *Environ. Sci. Technol.*, 2009, **43**, 157-162.

22. R. Liu, P. Wang, X. F. Wang, H. G. Yu and J. G. Yu, *J. Phys. Chem. C*, 2012, **116**, 17721-17728.

23. G. Palmisano, V. Augugliaro, M. Pagliaro and L. Palmisano, *Chem. Commun.*, 2007, 3425-3437.

24. A. Tanaka, K. Hashimoto and H. Kominami, *J. Am. Chem. Soc.*, 2012, **134**, 14526-14533.

25. D. Tsukamoto, M. Ikeda, Y. Shiraishi, T. Hara, N. Ichikuni, S. Tanaka and T. Hirai, *Chem. Eur. J.*, 2011, **17**, 9816-9824.

26. Y. H. Zhang and Y. J. Xu, *RSC Adv.*, 2014, **4**, 2904-2910.

27. Y. H. Zhang, N. Zhang, Z. R. Tang and Y. J. Xu, *Chem. Sci.*, 2013, **4**, 1820-1824.

28. S. Yurdakal, G. Palmisano, V. Loddo, V. Augugliaro and L. Palmisano, *J. Am. Chem. Soc.*, 2008, **130**, 1568-1569.

29. S. Yurdakal, G. Palmisano, V. Loddo, O. Alagoz, V. Augugliaro and L. Palmisano, *Green Chem.*, 2009, **11**, 510-516.

30. L. Palmisano, V. Augugliaro, M. Bellardita, A. Di Paola, E. G. Lopez, V. Loddo, G. Marci, G. Palmisano and S. Yurdakal, *ChemSusChem*, 2011, **4**, 1431-1438.

31. Z. Y. Zhong, J. Y. Lin, S. P. Teh, J. Teo and F. M. Dautzenberg, *Adv. Funct. Mater.*, 2007, **17**, 1402-1408.

32. J. L. Wang, Y. Yu and L. Z. Zhang, *Appl. Catal. B: Environ.*, 2013, **136-137**, 112-121.

33. Y. Zhou, Z. P. Tian, Z. Y. Zhao, Q. Liu, J. H. Kou, X. Y. Chen, J. Gao, S. C. Yan and Z. G. Zou, *ACS Appl. Mater. Interfaces*, 2011, **3**, 3594-3601.

34. J. Y. Zhang, Y. H. Wang, J. Zhang, Z. Lin, F. Huang and J. G. Yu, *ACS Appl. Mater. Interfaces*, 2013, **5**, 1031-1037.

35. Z. J. Zhang, W. Z. Wang, L. Wang and S. M. Sun, *ACS Appl. Mater. Interfaces*, 2012, **4**, 593-597.

36. X. G. Zhang, X. B. Ke and H. Y. Zhu, *Chem. Eur. J.*, 2012, **18**, 8048-8056.

37. S. Sakthivel, M. Janczarek and H. Kisch, *J. Phys. Chem. B*, 2004, **108**, 19384-19387.

38. K. M. Parida, N. Sahu, A. K. Tripathi and V. S. Kamble, *Environ. Sci. Technol.*, 2010, **44**, 4155-4160.

39. M. Valden, X. Lai and D. W. Goodman, *Science*, 1998, **281**, 1647-1650.

40. M. Haruta and M. Date, *Appl. Catal. A: Gen.*, 2001, **222**, 427-437.

RSC Advances Accepted Manuscript

41. S. Martha, K. H. Reddy, N. Biswal and K. M. Parida, *Dalton Trans.*, 2012, **41**, 14107-14116.

42. K. Hashimoto, Y. Masuda and H. Kominami, *ACS Catal.*, 2013, **3**, 1349-1355.

43. Y. L. Zhang, Q. Xiao, Y. S. Bao, Y. J. Zhang, S. Bottle, S. Sarina, B. Zhaorigetu and H. Y. Zhu, *J. Phys. Chem. C*, 2014, **118**, 19062-19069.

44. M. S. Elovitz and U. V. Gunten, *Ozone Sci. Eng.*, 1999, **21**, 239-260.

45. W. Li, D. Li, Y. Lin, P. Wang, W. Chen, X. Fu and Y. Shao, *J. Phys. Chem. C*, 2012, **116**, 3552-3560.

46. A. Primo, T. Marino, A. Corma, R. Molinari and H. García, *J. Am. Chem. Soc.*, 2011, **133**, 6930-6933.

47. M. Zhang, Q. Wang, C. C. Chen, L. Zang, W. H. Ma and J. C. Zhao, *Angew. Chem., Int. Ed.*, 2009, **48**, 6081-6084.

48. H. B. Fu, W. Zhang, S. C. Zhang, Y. F. Zhu and J. C. Zhao, *J. Phys. Chem. B*, 2006, **110**, 3061-3065.

49. J. N. Schrauben, R. Hayoun, C. N. Valdez, M. Braten, L. Fridley and J. M. Mayer, *Science*, 2012, **336**, 1298-1301.

50. A. Tanaka, S. Sakaguchi, K. Hashimoto and H. Kominami, *ACS Catal.*, 2013, **3**, 79-85.

51. A. Ishikawa, T. Takata, J. N. Kondo, M. Kara, H. Kobayashi and K. Domen, *J. Am. Chem. Soc.*, 2002, **124**, 13547-13553.

52. P. M. Wood, *Biochem. J.*, 1988, **253**, 287-289.

53. X. Fu, J. Long, X. Wang, D. Y. Leung, Z. Ding, L. Wu, Z. Zhang, Z. Li and X. Fu, *Int. J. Hydrogen Energy*, 2008, **33**, 6484-6491.

54. J. Lee, T. Javed, T. Skeini, A. O. Govorov, G. W. Bryant and N. A. Kotov, *Angew. Chem. Int. Ed.*, 2006, **45**, 4819-4823.

RSC Advances Accepted Manuscript